Published in final edited form as:
Cell Rep. 2023 September 26; 42(9): 113088. doi:10.1016/j.celrep.2023.113088.

VIP interneurons regulate cortical size tuning and visual perception

Katie A. Ferguson[1], **Jenna Salameh**[1], **Christopher Alba**[1], **Hannah Selwyn**[1], **Clayton Barnes**[1], **Sweyta Lohani**[1], **Jessica A. Cardin**[1,2,*]

[1]Department of Neuroscience, Kavli Institute for Neuroscience, Wu Tsai Institute, Yale University School of Medicine, New Haven, CT 06510, USA

[2]Lead contact

SUMMARY

Cortical circuit function is regulated by extensively interconnected, diverse populations of GABAergic interneurons that may play key roles in shaping circuit operation according to behavioral context. A specialized population of interneurons that co-express vasoactive intestinal peptides (VIP-INs) are activated during arousal and innervate other INs and pyramidal neurons (PNs). Although state-dependent modulation of VIP-INs has been extensively studied, their role in regulating sensory processing is less well understood. We examined the impact of VIP-INs in the primary visual cortex of awake behaving mice. Loss of VIP-IN activity alters the behavioral state-dependent modulation of somatostatin-expressing INs (SST-INs) but not PNs. In contrast, reduced VIP-IN activity globally disrupts visual feature selectivity for stimulus size. Moreover, the impact of VIP-INs on perceptual behavior varies with context and is more acute for small than large visual cues. VIP-INs thus contribute to both state-dependent modulation of cortical activity and sensory context-dependent perceptual performance.

Graphical abstract

---

[*]Correspondence: jess.cardin@yale.edu.

AUTHOR CONTRIBUTIONS
K.A.F., S.L., and J.A.C. designed the experiments. K.A.F., J.S., C.A., and H.S. collected the data. K.A.F. analyzed the data. K.A.F. and J.A.C. wrote the manuscript.

SUPPLEMENTAL INFORMATION
Supplemental information can be found online at https://doi.org/10.1016/j.celrep.2023.113088.

DECLARATION OF INTERESTS
The authors declare no competing interests.

INCLUSION AND DIVERSITY
We support inclusive, diverse, and equitable conduct of research.

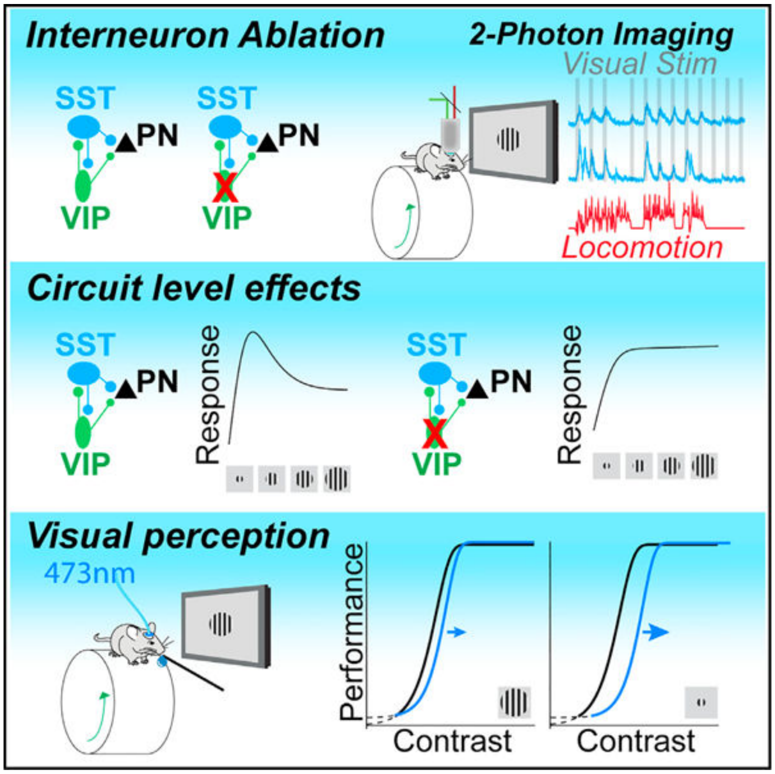

In brief

Ferguson et al. show that VIP interneurons regulate cortical visual feature selectivity. Loss of VIP interneurons decreases state-dependent modulation of SST interneurons and reduces visual tuning in SST interneurons and excitatory pyramidal neurons. Suppression of VIP interneurons has a size-dependent impact on perception of visual stimuli.

INTRODUCTION

The function of local circuits in the neocortex is shaped by the activity of a diverse set of GABAergic interneurons with distinct intrinsic properties, connectivity, and synaptic dynamics.[1–4] Recent work has highlighted the role of a specialized population of vasoactive intestinal peptide-expressing interneurons (VIP-INs) in the state-dependent regulation of cortical activity.[5–7] VIP-INs are depolarized by acetylcholine[6,8–11] and are active during periods of high arousal, behaviorally relevant input,[12,13] and locomotion.[5–7,14] Their influence on local circuit operations may thus be selectively exerted according to behavioral context.

The influence of VIP-INs on the surrounding circuit is largely thought to arise through their robust inhibition of another population of GABAergic INs that co-express the peptide somatostatin (SST-INs).[2,15,16] VIP-IN inhibition of SST-INs leads to disinhibition of local excitatory pyramidal neurons (PNs), causing amplification of PN activity.[6,12,17–22] VIP-INs also receive inhibition from SST-INs and parvalbumin-expressing INs (PV-INs)[2,23,24] and directly inhibit both local PV-INs[25] and the dendrites of local PNs.[26–30] Inhibitory-to-inhibitory synaptic interactions among VIP-, SST-, and PV-INs may maintain a balance between inhibition and disinhibition and likely play a role in stabilizing the operation of cortical circuits.[31–36]

Although the state-dependent modulation of VIP-INs has been extensively characterized,[5–7,37] their impact on cortical sensory encoding is less well understood. The complex interactions among cortical INs may permit sensory context-dependent engagement of distinct modes of inhibitory modulation of local cortical circuits.[21] In mouse primary visual cortex, where IN response properties have been extensively studied, VIP-INs have small receptive fields.[5,38] Recent work found that VIP-INs respond primarily to small, low-contrast visual stimuli and are suppressed in response to larger, more salient stimuli.[32,39] VIP-IN inhibition of SST-INs depends on visual context and is robust when stimulus center and surround differ but may be reduced when center and surround match.[40] Moreover, manipulation of VIP-IN activity can modulate overall levels of cortical activity[18] and some visual response properties of PNs.[41] However, the contributions of interactions between VIP and SST INs to visual tuning of local PNs remains unclear. Furthermore, the degree to which VIP-IN activity regulates visual perception is unknown. Here, we use short- and long-term manipulation of VIP-INs to examine their role in shaping both the behavioral state-dependent visual feature selectivity of cortical SST-INs and PNs and visual perceptual behavior.

RESULTS

Targeted removal of VIP-INs in V1

VIP-INs are activated at the onset of locomotion and other high arousal states, suggesting that they contribute to state-dependent modulation of local circuit activity. We tested the role of VIP-INs in regulating the state modulation of local neurons, using mouse primary visual cortex (V1) as a model of local circuit function. VIP-INs synapse on local SST-INs,[2,25,42] which provide dendritic inhibition to excitatory pyramidal cells (PNs).[43–45] However, VIP-INs also target other IN populations and directly inhibit PN dendrites.[26–30] Thus, to identify the impact of VIP inhibition on downstream targets in the local circuit, we used 2-photon imaging to measure the activity of either SST-INs or PNs in control and VIP-ablated animals (see STAR Methods). We selectively caused apoptotic cell death of VIP-INs via expression of a conditional viral construct carrying a genetically engineered caspase-3[46] (Figure 1A). Cell-type-specific expression of caspase caused rapid cell death in >75% of VIP-INs in the V1 within 2 weeks of viral injection (Figures S1A–S1D).

We expressed the calcium indicator GCaMP6 in SST-INs or PNs in layer 2/3 of the V1 and imaged each population in awake, head-fixed adult control and VIP-ablation mice (Figures 1 and S1) across waking behavioral states (Figures 1B and 1C). In controls, the majority of SST-INs exhibited increases in activity with high arousal, marked by the onset of locomotion (Figures 1D and 1E),[5–7] whereas PNs showed a more diverse profile (Figures 1G and 1H).[47,48] In the absence of VIP-INs, state-dependent modulation of spontaneous SST-IN activity was significantly enhanced (Figures 1D–1F), suggesting that VIP inhibition of SST-INs normally regulates the spontaneous activity of these cells. In contrast, loss of VIP-INs had no impact on the state-dependent regulation of PN activity (Figures 1G–1I).

Together, these data suggest that loss of VIP-INs has a strong impact on the regulation of SST-INs, but not PNs, by behavioral state.

Experimental data and computational modeling of cortical circuits suggest that inhibition plays a role in stabilizing local networks[31,33,34,36] and coordinating patterns of activity.[49–51] To examine the impact of VIP inhibition on the coordinated activity of local SST-INs and PNs, we presented repeated high-contrast visual stimuli and measured noise correlations[52] within each population. Loss of VIP-INs led to increased modulation of noise correlations among SST-INs, but not PNs, by behavioral state (Figures S1E–S1H; see STAR Methods).

VIP-IN loss disrupts visual response tuning

Previous work has found that VIP-INs are selectively activated by small visual stimuli[5,38] (but see Millman et al.[32]), suggesting that their impact on the surrounding local circuit may depend on visual context. We therefore tested the impact of VIP-IN ablation on the tuning of SST-INs and PNs for drifting grating stimuli of varying sizes (Figures 2A and 2B). In control animals, SST-INs exhibited broad tuning for stimulus size, with a preference for stimuli of 20°–30° in diameter (Figure 2A).[5,53] In contrast, PNs were selective for stimuli of ~10° in diameter and exhibited robust surround suppression that is thought to be mediated in part by SST-IN inhibition[53] (Figure 2B). In SST-INs, VIP ablation led to a reduction in the number of visually tuned cells (Figures S2A and S2B), to decreased size tuning (Figures 2A and 2C), and to a loss of surround suppression during quiescence (Figure 2D). In PNs, VIP ablation likewise led to reduced surround suppression across states (Figures 2B, 2E, 2F, S2C, and S2D). These changes were associated with a significant increase in the size of preferred stimuli for both SST-INs and PNs (Figures S2E–S2H). Similar results were observed when both tuned and untuned cells were included in the analysis (Figures S2I–S2L). Together, these results suggest that VIP-IN activity in the V1 normally serves to shape surround suppression and enhance selectivity for small stimuli.

Perturbation of VIP-INs changes visual perceptual performance

Our findings suggest that VIP-INs function to shape visual responses of INs and PNs in the local V1 circuit. To examine how VIP-IN regulation of visual feature selectivity may contribute to perceptual behavior, we manipulated VIP-IN activity in the V1 during performance of a visual detection task in which head-fixed mice lick for water rewards in response to uncued presentations of contrast-varying stimuli (Figures 3A and 3B). Because the extended training times required for expert task performance (see STAR Methods) might permit the emergence of compensatory changes following long-term loss of VIP-INs, we assessed the impact of both short-term (Figures 3 and S3A–S3K) and long-term (Figures S3L–S3P) manipulation of VIP-IN activity in the V1.

We expressed a conditional viral construct carrying the light-activated suppressive opsin GtACR2[54] either globally in all cells or selectively in VIP-INs in the V1. Light stimulation to suppress target populations was calibrated using global expression of GtACR2 in the V1 neural population (Figures S3A–SF). Light stimulation in control animals injected with saline had no impact on performance of the contrast detection task (Figure 3C). Cell-type-specific suppression of VIP-IN activity by activation of GtACR2 with 473 nm light caused a rightward shift of the psychophysical performance curve on the task, leading to an increase in the contrast detection threshold (C_{50}; Figure 3D). Ablation of VIP-INs likewise caused a rightward shift in the psychometric performance curve and an overall increase in the C_{50} (Figures S3L–SP) that was particularly prominent during periods of quiescence (Figure S3O). Neither short-nor long-term manipulations of VIP-INs altered false alarm rates or running behavior (Figures 3E, S3N, and S3P).

Because ablation of VIP-INs had a substantial impact on the size tuning of SST-INs and PNs, we hypothesized that the impact of VIP-IN manipulation on visual perceptual performance may depend on stimulus context. Consistent with our size-tuning results, optogenetic suppression of VIP-INs had a substantially larger impact on the detection threshold for small than large stimuli (Figures 3F, 3G, S3J, and S3K). Overall, these results indicate a role for VIP-INs in regulating the visual feature selectivity of downstream SST-INs and PNs and ultimately in regulating perceptual thresholds for visual stimuli in a size-dependent manner.

DISCUSSION

Our results reveal a key role for VIP-INs in regulating cortical visual feature selectivity. We find that VIP-IN ablation causes dysregulation of state-dependent modulation of spontaneous activity in SST-INs but not in PNs. We also find that loss of VIP-INs leads to reduced selectivity for visual stimulus size in SST-INs and PNs. We further find that loss or suppression of VIP-IN activity increases the perceptual threshold for detection of visual stimuli. The behavioral impact of VIP-IN manipulation is substantially greater for small than large stimuli, suggesting that the role of VIP-INs in the local V1 circuit varies with visual context.

Imaging in the V1 of awake control animals revealed robust state-dependent modulation of the activity of both SST-INs and PNs. Several previous studies have found that VIP-INs are activated at the onset of locomotion[5–7] and in response to punishment or unexpected stimuli.[12,13] VIP-INs receive direct innervation from basal forebrain cholinergic projection neurons[6] and are depolarized by application of acetylcholine,[6,8–11] suggesting that they may serve as one avenue by which state information reaches primary cortical circuits. These findings gave rise to the “disinhibition model,” where the state-dependent activation of VIP-INs leads to disinhibition of PNs during arousal and locomotion by suppressing intermediary SST-INs.[6,19] Consistent with this view, we found that ablation of VIP-INs caused an enhancement of locomotion modulation of spontaneous activity in local SST-INs, suggesting that VIP-INs normally regulate the degree to which SST-INs are activated during arousal even in the absence of strong visual drive.[32] Despite this increase in SST-IN activity, loss of VIP-INs did not change the state modulation of the PN population. Hippocampal VIP-INs comprise several functionally distinct subpopulations, including calretinin-expressing cells that selectively target SST-INs and cholecystokinin-expressing (CCK) cells that directly inhibit the dendrites of PNs.[28–30] Although these subpopulations remain to be fully investigated in the neocortex, anatomical and *ex vivo* synaptic physiology data suggest that VIP-INs synapse on both SST-INs and on the dendrites of local PNs.[26,27] Combined loss of both direct inhibition of PNs and disinhibition via SST-INs following

VIP-IN ablation may thus lead to minimal change in PN activity. Alternatively, it is possible that loss of VIP-INs leads to compensatory changes selectively in PNs.

In previous work, we found that developmental perturbation of VIP-INs, which caused a loss of VIP-to-SST inhibitory synapses, likewise enhanced state-dependent modulation in SST-INs.[14] Developmental perturbation of VIP-INs further abolished state-dependent modulation and substantially impaired visual responses in PNs.[14,55] In contrast, adult VIP-IN ablation had no impact on PN state modulation but did affect feature selectivity. Together, these results suggest distinct roles for VIP-INs in the developing and mature cortex.

Cortical networks exhibit dynamic fluctuations across a range of spatial and temporal scales.[52] Slow fluctuations, often measured as noise correlations, are a measure of shared variability and can provide insight into functional connectivity,[47,56] information encoding, and transmission.[52,57] Previous work has suggested that inhibition controls the degree to which neural variability is correlated across a cortical population.[58] Estimating noise correlations from calcium imaging data presents several challenges. Calcium indicators introduce low-pass filtering of neural spiking activity, introducing biases that can be ameliorated by deconvolution.[59] However, inferring spikes from calcium transients is complex,[60] partially due to low sensitivity to single action potential events,[61] and the spike-to-fluorescence transform can vary across populations.[62] Furthermore, correlations can be biased by comparing samples with mismatched event rates.[52] To partially account for these factors, we estimated noise correlations from deconvolved data matched for mean activity rates. We found that loss of VIP-INs enhanced the state-dependent modulation of noise correlations within the SST-IN population, suggesting that inhibition from VIP-INs normally serves to regulate noise correlations of other INs . In contrast, we found no consistent impact on PN noise correlations. These results suggest that slow fluctuations in the PN population may be stabilized by other network influences, such as their tight coupling with the fast-spiking, PV-IN population.

Unlike the differential impact of VIP-IN ablation on state-dependent spontaneous SST-IN and PN activity, loss of VIP-INs led to similar changes in the visual responses of both populations. Both SST-INs and PNs exhibited loss of surround suppression, and PNs showed an increase in preferred stimulus size, following VIP-IN ablation. Previous work has found that SST-INs, which have large receptive fields and receive extensive horizontal cortico-cortical synaptic input, contribute to surround suppression in PNs.[53] VIP-IN inhibition of SST-INs regulates the sensitivity of PNs to visual stimulus features in the surround.[40] We found that, despite their small receptive fields,[5,38] VIP-INs contribute to selectivity for stimulus size in SST-INs, suggesting that inhibitory synaptic interactions may likewise mediate surround suppression in IN populations. Alternatively, it is possible that these effects result from a mix of direct and indirect effects of VIP-IN inhibition in the local cortical circuit. The loss of tuning and the shift toward decreased surround suppression in SST-INs following VIP-IN ablation were associated with a similar shift and increased preferred stimulus size in local PNs. The effects of VIP-IN ablation on size tuning were observed across quiescent and aroused behavioral states, suggesting that the impact of VIP-INs on visual tuning may be independent from their role in state-dependent regulation of spontaneous activity. Overall, our results suggest that VIP-INs robustly regulate size tuning in the V1 circuit. However, these effects could be mediated in part via network interactions that do not include SST-INs. The synaptic mechanisms by which VIP-INs promote tuning for smaller stimuli during visually driven activity patterns thus remain to be further explored.

In good agreement with previous work,[63] we found that suppression of VIP-IN activity in V1 led to an increased perceptual threshold for visual contrast detection in behaving mice. Both short- and long-term suppression of VIP-IN activity increased perceptual thresholds without affecting false alarm rates or locomotion. However, the behavioral impact of VIP-IN suppression was greatly enhanced for small compared with large visual stimuli, suggesting that reduced PN size tuning in the absence of VIP-IN activity selectively impairs the animal’s ability to detect small stimuli. In addition, because the influence of VIP inhibition on surrounding SST-INs is relatively local,[20] VIP-IN suppression and consequent loss of feature selectivity may exert less impact on the pooled circuit responses to larger stimuli. Overall, we observed more modest impact of VIP-IN manipulation during locomotion than quiescence, potentially due to floor effects on the low perceptual thresholds during locomotion trials. Together, our results indicate that VIP-INs play a substantial role in regulating cortical feature selectivity and that their impact on sensory processing varies with visual context.

Limitations of the study

In this study, we used short- and long-term manipulations to reveal a role for VIP-INs in regulating the spontaneous and sensory-evoked activity of SST-INs and PNs in V1 circuits. We found that ablating VIP cells led to changes in state-dependent modulation of SST-INs and loss of selectivity for stimulus size in both SST-INs and PNs. Using ablation and optogenetic manipulations, we further found that VIP-INs regulate visual perceptual performance in a stimulus size-dependent manner. Because long-term loss of VIP-INs could lead to compensatory changes in local cortical circuits, future work should more extensively explore the impact of VIP-IN inhibition on local circuits using optogenetics and imaging approaches. It will likewise be important in future experiments to continue to examine the real-time impact of VIP-INs during perceptual behavior using simultaneous optogenetics and cellular recording approaches. Additional experimental manipulations will be necessary to determine the mechanisms by which the loss of size tuning caused by VIP-IN suppression interacts with the spatial spread of VIP-IN influence in the local circuit. In addition, although our results were highly consistent across animals and showed large effect sizes, the number of animals used for behavioral experiments in the current study should be increased in future work.

Because VIP-INs are sparse, presenting a challenge for targeted electrophysiological recordings, we performed an optogenetic calibration using recordings of the general V1 neural population to ensure that light stimulation fell within a physiologically reasonable range. Using light pulses in that range, we found that optogenetic suppression of VIP cells on random task trials significantly altered perceptual behavior. However, in the future, it would be interesting to perform simultaneous 2-photon imaging and optogenetic manipulations to confirm the real-time impact of optogenetic suppression of VIP cells. Such experiments may provide further insight into the relationship between VIP-INs and their synaptic targets during sensory processing in primary cortical circuits.

STAR★METHODS

RESOURCE AVAILABILITY

Lead contact—Further information and requests for resources and reagents should be directed to and will be fulfilled by the lead contact, Jessica Cardin (jess.cardin@yale.edu).

Materials availability—This study generated no new reagents or materials.

Data and code availability

- Data reported in this paper and any additional information required are available from the lead contact upon request.
- All original code has been deposited at Zenodo and is publicly available as of the date of publication. The DOI is listed in the key resources table.
- Any additional information required to reanalyze the data reported in this paper is available from the lead contact upon request.

EXPERIMENTAL MODEL AND STUDY PARTICIPANT DETAILS

Animals—All animal handling and maintenance was performed according to the regulations of the Institutional Animal Care and Use Committee of the Yale University School of Medicine. Adult male and female C57BL/6J VIP-IRES-Cre$^{+/0}$ (Jax stock no. 031628), Emx1-IRES-Cre$^{+/0}$ (Jax stock no. 005628), VIP-IRES-Cre$^{+/0}$ mice crossed with Sst-IRES-Flp$^{+/0}$ (Jax stock no. 031629) mice, VIP-IRES-Cre$^{+/0}$ mice crossed with Ai9$^{F/0}$ (Jax stock no. 007909), VIP-IRES-Cre$^{+/0}$ crossed with Sst-IRES-Flp$^{+/0}$, and Sst-IRES-Cre$^{+/0}$ (Jax stock no. 018973) crossed with Ai148$^{F/0}$ (Ai148(TIT2L-GC6f-ICL-tTA2)-D, Jax stock no. 030328) mice were kept on a 12h light/dark cycle, provided with food and water *ad libitum*, and housed individually following headpost implants. Imaging experiments were performed during the light phase of the cycle. Twenty-two male and fifteen female mice ages P90-P180 were used in this study. Littermates of the same sex were randomly assigned to experimental groups.

METHOD DETAILS

Surgical procedures—Surgeries were performed in adult mice (P90–P180) in a stereotaxic frame, anesthetized with 1–2% isoflurane mixed with pure oxygen. Injections were made via beveled glass micropipette at a rate of 40–60 nL/min into the primary visual cortex (V1) at a depth of L2/3 (~350 μm) (QSI, Stoelting Co.). For imaging experiments, we injected 200nL of adenoassociated virus (AAVdj-ef1a-fDIO-GCaMP6m (plasmid gift of K. Deisseroth lab, Stanford), AAV5-Syn-GCaMP6s (Addgene # 100843), or AAV5-Syn-FLEX-GCaMP6s (Addgene # 100845); diluted to a titer of 10^12) unilaterally at three sites (in mm from bregma): AP 3.5, ML 1.5, DV 0.4; AP 3, ML 2, DV 0.4; AP 2.5, ML 2.5, DV 0.4. We also injected 1 μL of either the Cre-dependent Caspase-3 virus (AAV5 ef1α-Flex-taCasP3-TEVP; UNC Vector Core) or saline into V1 (in left V1 for imaging experiments, and bilaterally for behavioral experiments, 2–2.5 mm lateral and 3.5–4.0 mm posterior from bregma). For behavioral optogenetic experiments, we bilaterally (2–2.5 mm lateral and 3.5–4.0 mm posterior from bregma) injected 1 μL of the conditional GtACR2 virus (AAV1-hSyn1-SIO-stGtACR2-FusionRed, Addgene #105677), or 1uL saline injection for controls. After injection, pipettes were left in the brain for 5–10 min to prevent backflow.

For headpost implantation, mice were anesthetized with isoflurane and the scalp was cleaned with Betadine solution. An incision was made at the midline and the scalp resected to each side to leave an open area of the skull. After cleaning the skull and scoring it lightly with a surgical blade, a custom titanium head post was secured with C&B-Metabond (Butler Schein) with the left V1 centered. Two skull screws (McMaster-Carr) were placed at the right anterior and posterior poles (bilateral to the injection site). A 3 mm^2 craniotomy was made over the left V1. A glass window made of a 3 mm^2 rectangular inner coverslip adhered with an ultraviolet-curing adhesive (Norland Products) to a 5 mm round outer coverslip (both #1, Warner Instruments) was inserted into the craniotomy and secured to the skull with Cyanoacrylate glue (Loctite). A circular ring was attached to the titanium headpost with glue, and additional Metabond was applied to cover any exposed skull and to cover each skull screw. For the behavioral experiments, two skull screws (McMaster-Carr) were placed at the right anterior and posterior poles (bilateral to the injections/cranial window). Two nuts (McMaster-Carr) were glued in place over the bregma point with cyanoacrylate and secured with C&B-Metabond (Butler Schein). The Metabond was extended along the sides and back of the skull to cover each screw. For optogenetics experiments, two fiber-optic cannulas were lowered directly over the bilateral virus injection sites and secured with dental cement to allow for the delivery of light directly onto the surface of the cortex during the behavioral task. Analgesics were given immediately after surgery (5 mg/kg Carprofen and 0.05 mg/kg Buprenorphine) and on the two following days to aid recovery. Mice were given a course of antibiotics (Sulfatrim, Butler Schein) to prevent infection and were allowed to recover for 3–5 days following implant surgery before beginning wheel training.

Histology—Following experiments, animals were given a lethal dose of sodium pentobarbital and perfused intracardially with 0.9% saline followed by cold 4% paraformaldehyde in 0.1 m sodium phosphate buffer. For the Caspase-3 virus efficacy and timeline experiments, VIP-Cre$^{+/0}$;Ai9F$^{/0}$ animals were perfused 10, 14, and 21 days after unilateral injection of the AAV-ef1α-Flex-taCasP3-TEVP virus. Brains were removed and fixed in 4% PFA/PBS solution for 24 h and subsequently stored in PBS. Tissue was sectioned at 40μm using a vibrating blade microtome, mounted, and visualized by light microscopy. Widefield images were acquired on an Olympus BX53 fluorescence microscope. In a subset of cases, confocal images were taken with a Zeiss LSM 900.

To minimize counting bias we compared sections of equivalent bregma positions, defined according to the Mouse Brain atlas (Franklin and Paxinos, 2013). The total number of cells expressing tdTomato (from the Ai9 reporter mouse line) were counted for a defined optical area within V1. Cell counting was performed manually using a standardized 100 μm x 100 μm grid overlay to determine the average VIP cell density in layers 2/3 of V1 across three consecutive sections. The percentages of VIP interneurons were calculated as a ratio between the total number of tdTomato$^+$ cells in the injected area over the total number of tdTomato$^+$ cells on the contralateral control side.

In vivo calcium imaging—All imaging was performed during the second half of the light cycle in awake, behaving mice that were head-fixed so that they could freely run on a cylindrical wheel.[14,47,68] A magnetic angle sensor (Digikey) attached to the wheel continuously monitored wheel motion. Mice received at least three wheel-training habituation sessions before imaging to ensure consistent running bouts. The face (including the pupil and whiskers) was imaged with a miniature CMOS camera (Blackfly s-USB3, Flir) with a frame rate of 10 Hz.

Imaging was performed using a resonant scanner-based two-photon microscope (MOM, Sutter Instruments) coupled to a Ti:Sapphire laser (MaiTai DeepSee, Spectra Physics) tuned to 920 nm for GCaMP6. Emitted light was collected using a 25×1.05 NA objective (Olympus). Mice were placed on the wheel and head-fixed under the microscope objective. To prevent light contamination from the display monitor, the microscope was enclosed in blackout material that extended to the headpost. Images were acquired using ScanImage 4.2 at 30 Hz, 512x512 pixels. Imaging of layer 2/3 was performed at 150–350 μm depth relative to the brain surface. For each mouse, 1–4 fields of view were imaged. Visual stimulation, wheel position, and $Ca2+$ imaging microscope resonant scanner frame ticks, were digitized (5 kHz) and collected through a Power 1401 (CED) acquisition board using Spike 2 software. During each session, spontaneous activity was collected for 10 min before the series of visual stimuli were presented, and 10 min after (20 min total) as the mouse freely moved on the wheel in front of a mean-luminance gray screen.

Visual stimulation—Visual stimuli were generated using Psychtoolbox-3 in MATLAB and presented on a gamma-calibrated LCD monitor (17 inches) at a spatial resolution of 1280 x 960, a real-time frame rate of 60Hz, and a mean luminance of 30 cd/m^2 positioned 20 cm from the right eye. Stimuli had a temporal frequency of 2 Hz, spatial frequency of 0.04 cycles per degree, and orientation of 180°. To center stimuli on the receptive field, 100% contrast stimuli were randomly presented in nine 3x3 sub-regions to identify the location that evoked the largest population response in the field of view. The screen was centered, and the process was repeated until a center was identified. Stimuli in each session were randomized and presented in blocks with a fixed duration of 2 s and an interstimulus interval of 5 s, with a mean-luminance gray screen between stimuli. For size tuning, the visual angle was linearly spaced from 0° to 80° in diameter in steps of 10°, where each size was presented 45 times.

Visual detection task—Mice were trained to perform a visual contrast detection task while head-fixed on a wheel. Mice were placed on a water-controlled schedule with careful weight monitoring and habituated to head fixation. Once mice were stabilized at 83–86% of their starting weight and exhibited consistent running bouts on the wheel, they were trained to lick a waterspout in response to the presentation of a high-contrast (100%), full-screen stimulus of 1 s duration (temporal frequency: 2Hz; spatial frequency: 0.05 cycles/degree). Successful detection of the visual stimulus resulted in a reward and prolonged the presentation for an additional 1 s (total 2 s). When a performance criterion of >95% hit rates and <10% false alarm rates was reached (~5–10 days), they were moved to a psychometric version of the task where the stimulus contrast varied randomly across trials. Contrast was selected on each trial from the series: 0, 0.35, 0.5, 0.75, 1, 2, 5, 10, 20, 100%. To determine how visual perception is regulated in a size-dependent manner, either small (20° diameter) or large (100° diameter; full screen) stimuli were used throughout the duration of the task. Stimulus and non-stimulus (0% contrast) trials were presented at a one-to-one ratio. To maintain motivation in the task, high contrasts were over sampled such that stimuli greater than 1.5% contrast made up 70% of the displayed (non-zero) stimuli. The response window for a correct response (hit) began at stimulus onset and lasted for 1 s. Hits were rewarded with a small (3 μL) drop of water. The inter-trial interval (ITI) for both stimulus and non-stimulus trials was drawn from an exponential distribution to ensure a flat hazard rate, with a mean ITI of 4 s, a minimum ITI of 1.5 s, and a maximum ITI of 10 s. False alarms were punished with an extended inter-trial interval by re-sampling the ITI starting from the time of the false alarm. Mice performed the task daily for 45 min per session, over 10 sessions. Mice began the contrast detection task no earlier than 22 days following virus injection.

To acutely inhibit VIP-INs, fiber-optic cannulas were surgically implanted at the injection sites, bilaterally in V1. The light was delivered through a fiber coupled 473nm LED laser to the cortical surface at an intensity of 75 mW/mm^2 (Cardin, 2010). Optogenetic stimulation trials were randomly assigned to 50% of the stimulus and non-stimulus trials, where a 2.25s pulse of light was activated 250ms preceding the onset of the visual stimulus.

Data analysis

Wheel position and changepoints: Wheel position was determined from the output of the linear angle detector. The circular wheel position variable was first transformed to the $[-\pi, \pi]$ interval. The phases were then circularly unwrapped to get running distance as a linear variable, and locomotion speed was computed as a differential of distance (cm/s). A change-point detection algorithm detected locomotion onset/offset times based on changes in standard deviation of speed. Locomotion onset or offset times were estimated from periods when the moving standard deviations, as determined in a 0.5s window, exceeded or fell below an empirical threshold of 0.1. Locomotion trials were required to have average speed exceeding 0.5 cm/s and last longer than 1 s. Quiescence trials were required to last longer than 2 s and have an average speed <0.5 cm/s.

Quantification of calcium signals—Analysis of imaging data was performed using ImageJ and custom routines in MATLAB (The Mathworks). Motion artifacts and drifts in the Ca^{2+} signal were corrected with the moco plug-in in ImageJ (Dubbs et al., 2016), and regions of interest (ROIs) were selected as previously described (Chen et al., 2013). All pixels in each ROI were averaged as a measure of fluorescence, and the neuropil signal was subtracted (Chen et al., 2013; Lur et al., 2016; Tang et al., 2020). $\Delta F/F$ was calculated as $(F-F_0)/F_0$, where F_0 was the lowest 10% of values from the neuropil-subtracted trace for each session.

Modulation index—For modulation by behavioral state without visual stimulation, we used the spontaneous periods recorded as described above and selected locomotion trials that lasted 5 s or longer and quiescent trials that lasted 30 s or longer. To determine whether Ca^{2+} activity was altered during behavioral state transitions, $\Delta F/F(t)$ from [0,5]s after locomotion onset ($Ca_{L\text{-}ON}$) was compared with $\Delta F/F(t)$ from [20,25]s after locomotion offset (Ca_Q) by computing a modulation index (MI), where $MI = (Ca_{L\text{-}ON} - Ca_Q)/(Ca_{L\text{-}ON} + Ca_Q)$. A minimum of 5s of quiescence after this period [25,30]s was required to prevent anticipatory effects on Ca_Q. To ascertain the significance of this MI, we used a shuffling method in which the wheel trace was randomly circularly shifted relative to the fluorescence trace 1,000 times. Cells were deemed significantly modulated if their MI was outside of the 95% confidence interval of the shuffled comparison.

Visual responses—Visual response amplitude was calculated as the z-scored change in fluorescence (z-scored F) during the 2s visual stimulus compared to the 1s baseline before the stimulus. To separate effects of state, the mouse was required to be running (or sitting) during the full duration of the 1s baseline and the 2 s visual stimulation. To determine if cells were visually responsive, a bootstrapped null distribution was generated by sampling with replacement from each cell's pre-stimulus baseline. Cells were deemed visually responsive if their mean responses to their preferred stimulus (100% contrast or preferred stimulus size) was outside of the 95% bootstrapped confidence interval in at least one of the two behavioral state conditions (quiescence or locomotion).

Size tuning of all cell types, and particularly of SST-INs, prefer larger stimulus sizes when not well centered (Dipoppa et al., 2018). After centering our stimuli, we only included cells in our size tuning analysis that were both visually responsive and tuned and thus well matched to the visual stimuli. To identify tuned cells, size tuning curves were fitted by least-squares with the difference in error functions (erf):

$$f(s) = R[erf(s/\sigma_1) - k\, erf(s/\sigma_2)] + b$$

where s is the size of the stimulus, and the free parameters are R, k, b, s_1 and s_2. Tuned cells were defined as visually responsive cells whose fit curve was not monotonically increasing or decreasing. To compute the surround suppression index (SSI), we normalized the z-scored F of tuned cells to their peak and computed the difference in normalized activity at the preferred size and the largest stimuli (Adesnik et al., 2012). SSI index was computed using the preferred size based on stimuli presented, not on the fit data, to prevent it from being affected by goodness of fit.

Pairwise correlations were determined as trial-by-trial fluctuations in response strength between cells to high contrast stimuli (80–100%). To compute these noise correlation coefficients, either the $\Delta F/F_0$ traces were used, or the spike traces for each cell were deconvolved using a first order autoregressive model (OASIS,[69]), and spike times were selected as those that exceeded 3 standard deviations. State conditions were separated ($v = 0$ stationary, $v = 1$ running). For each trial in state v for each of the [80, 90, 100]% contrast trials (stimulus s) (t_{vs}) we calculated the average number of spikes (r) for each cell (i) in cell class I: $\bar{r}_{ivs} = \langle r(t_{vs}, i) \rangle$, where $t_{vs} \in \{v, s\}$ and $i \in \{c\}$. As differences in firing rates can markedly affected measured noise correlations (Cohen and Kohn, 2011), in a subset of analyses firing rates between stationary and running conditions were mean-matched across cells using a threshold of 0.5 Hz. To do so, for each cell's locomotion firing rate, we identified a "paired" cell whose quiescence firing rate fell within the threshold. If none existed, we eliminated that cell. For each t_{vs} (trial in locomotion condition v with stimulus s) and for each i (cell), we subtracted the average response, $\Delta r_{ivs} = r(t_{vs}, i) - \bar{r}_{ivs}$, and pooled the trial-by-trial fluctuations across stimuli ($\Delta\ r_{iv}$). The Pearson's correlation of these spike count responses $\Delta\ r_{iv}$ across pairs of cells ($\rho_{ij,v}$ for cells i, j during condition v) was calculated.

Behavioral performance—We restricted the data used per session automatically as follows. First, we ensured that when the mice stopped performing at the end of a session, these data were not incorporated into the average. This was done by computing a 10-point moving average of the data. For the k-th trial, we then computed the average performance of the mouse (as hit_O) until the $(k\text{-}1)$-th trial. This average performance was computed starting from the trial where the mouse had obtained at least 10 rewards, to prevent poor performance at the start from influencing the average. (Note that the first ten trials in each session were 100% contrast trials). The last trial was defined as the trial at which the 10-point moving average of the hit rate (HR) fell below 75% of the mean performance up to that point and did not recover above this level anymore. We then computed the average HR for each contrast, and the average false alarm rate (FAR) from the non-stimulus (0% contrast) trials. In the optogenetic experiments, performance and FAR were further separated by the presence of the light stimulus ("light-off" or "light-on" trials). Sessions were removed from the analysis if the median light-off FAR or HR at the two lowest contrasts (0.35% and 0.5%) exceeded 40% or if the median light-off HR at the highest contrast (100%) was below 75%.

Performance was separated by arousal state, where locomotion states were indicated by any duration of locomotion in the 1s preceding the visual stimulation. As trials for each session were categorized by state and light stimulation (for the optogenetic experiments), and thresholds gleaned from psychometric curve fitting are sensitive to low trial numbers, we aggregated our trials across 10 sessions to optimize our fits. We fit the psychometric curves with a Weibull function using the *psignifit* toolbox in MATLAB, a software package which implements the maximum-likelihood method.[66] A 95% confidence interval was determined by the percentile bootstrap method implemented by *psignifit* based on 2000 simulations. The contrast detection threshold (C_{50}) was the lowest contrast that can be detected at least 50% of the time, scaled by the guess rate (lower asymptote) and lapse rate (upper asymptote) of the psychometric curve fits. We calculated the C_{50} *shift* by subtracting the C_{50} value for light-on trials from the C_{50} value for light-off trials to measure the difference in performance after inhibiting VIP-INs.

QUANTIFICATION AND STATISTICAL ANALYSES

We used mixed effect regression models for imaging data, due to its nested structure with multiple cells recorded within each mouse. We treated the experiment type (control or VIP-ablated) as the fixed effect, and the individuals (mice) were random effects. Since our experimental design was between-subject, we used the *lmefit* function in MATLAB to fit the intercepts of the random effects, with the response modeled as:

$$\text{response} \sim \text{experimentType} + (1 \mid \text{mouse} : \text{FoV})$$

which has the following mathematical form:

$$y_{ijk} = \beta_0 + \beta_1 x_{ijk} + u_i + b_{ij} + \epsilon_{ijk}$$

where y_{ijk} is the i^{th} observation for the j^{th} mouse in the k^{th} field of view. x_{ijk} is the experiment type (control or VIP-ablated) for the observation i of the j^{th} mouse and k^{th} field of view (FoV). β_0 is the intercept, β_1 is the effect of the experiment type, u_i is the random effect for the i^{th} observation, b_{ij} is the random effect for the i^{th} observation in the j^{th} mouse, and ϵ_{ijk} is the residual error for the i^th^ observation within the j^th^ mouse and k^{th} field of view. The random effects have prior distributions $u_i \sim N\left(0, \sigma_u^2\right)$ and $b_{ij} \sim N\left(0, \sigma_b^2\right)$, and the error term has the distribution $\epsilon_{ijk} \sim N\left(0, \sigma^2\right)$.

Since the surround suppression index and the preferred size were continuous bounded variables, we instead used a 0/1 inflated beta mixed effect regression model. For these data, preferred size was scaled to [0, 1] to represent the proportion of the size compared to maximum. Then we fit a 0/1 inflated beta mixed effect regression model using the *gamlss* package in R using the family “BEINF”.

For the behavioral data, given one psychometric curve fit per mouse, data was compared with a t test after a test for normality. Paired t-tests were used when comparing light-on and light-off trials, and unpaired t-tests were used when comparing across mice.

All of the details of the statistical tests used, including n’s and definition of center and dispersion, are provided in summary table of statistical tests. No tests were used to justify sample size, but sample sizes in the current study are comparable to several recent studies in behaving mice.[5,40,47,51]

Supplementary Material

Refer to Web version on PubMed Central for supplementary material.

ACKNOWLEDGMENTS

The authors thank all members of the Higley and Cardin laboratories for helpful input throughout all stages of this study. We thank Rima Pant for generation of adeno-associated virus (AAV) vectors and Quentin Perrenoud for guidance on the behavioral task design. This work was supported by funding from the NIH (R01EY022951 and R01MH113852 to J.A.C., K99EY030549 to K.A.F., and EY026878 to the Yale Vision Core), an award from the Kavli Institute of Neuro-science (to J.A.C.), the Ludwig Foundation (to J.A.C.), and a BBRF Young Investigator Grant (to K.A.F.).

REFERENCES

1. Fishell G, and Rudy B (2011). Mechanisms of inhibition within the telencephalon: "where the wild things are. Annu. Rev. Neurosci 34, 535–567. 10.1146/annurev-neuro-061010-113717. [PubMed: 21469958]
2. Pfeffer CK, Xue M, He M, Huang ZJ, and Scanziani M (2013). Inhibition of inhibition in visual cortex: the logic of connections between molecularly distinct interneurons. Nat. Neurosci 16, 1068–1076. 10.1038/nn.3446. [PubMed: 23817549]
3. Rudy B, Fishell G, Lee S, and Hjerling-Leffler J (2011). Three groups of interneurons account for nearly 100% of neocortical GABAergic neurons. Dev. Neurobiol 71, 45–61. 10.1002/dneu.20853. [PubMed: 21154909]
4. Tremblay R, Lee S, and Rudy B (2016). GABAergic Interneurons in the Neocortex: From Cellular Properties to Circuits. Neuron 91, 260–292. 10.1016/j.neuron.2016.06.033. [PubMed: 27477017]
5. Dipoppa M, Ranson A, Krumin M, Pachitariu M, Carandini M, and Harris KD (2018). Vision and Locomotion Shape the Interactions between Neuron Types in Mouse Visual Cortex. Neuron 98, 602–615.e8. 10.1016/j.neuron.2018.03.037. [PubMed: 29656873]
6. Fu Y, Tucciarone JM, Espinosa JS, Sheng N, Darcy DP, Nicoll RA, Huang ZJ, and Stryker MP (2014). A cortical circuit for gain control by behavioral state. Cell 156, 1139–1152. 10.1016/j.cell.2014.01.050. [PubMed: 24630718]
7. Pakan JM, Lowe SC, Dylda E, Keemink SW, Currie SP, Coutts CA, and Rochefort NL (2016). Behavioral-state modulation of inhibition is context-dependent and cell type specific in mouse visual cortex. Elife 5, e14985. 10.7554/eLife.14985. [PubMed: 27552056]
8. Askew CE, Lopez AJ, Wood MA, and Metherate R (2019). Nicotine excites VIP interneurons to disinhibit pyramidal neurons in auditory cortex. Synapse 73, e22116. 10.1002/syn.22116. [PubMed: 31081950]
9. Gasselin C, Hohl B, Vernet A, Crochet S, and Petersen CCH (2021). Cell-type-specific nicotinic input disinhibits mouse barrel cortex during active sensing. Neuron 109, 778–787.e3. 10.1016/j.neuron.2020.12.018. [PubMed: 33472037]
10. Porter JT, Cauli B, Tsuzuki K, Lambolez B, Rossier J, and Audinat E (1999). Selective excitation of subtypes of neocortical interneurons by nicotinic receptors. J. Neurosci 19, 5228–5235. 10.1523/JNEUROSCI.19-13-05228.1999. [PubMed: 10377334]
11. Ren C, Peng K, Yang R, Liu W, Liu C, and Komiyama T (2022). Global and subtype-specific modulation of cortical inhibitory neurons regulated by acetylcholine during motor learning. Neuron 110, 2334–2350.e8. 10.1016/j.neuron.2022.04.031. [PubMed: 35584693]
12. Pi HJ, Hangya B, Kvitsiani D, Sanders JI, Huang ZJ, and Kepecs A (2013). Cortical interneurons that specialize in disinhibitory control. Nature 503, 521–524. 10.1038/nature12676. [PubMed: 24097352]
13. Szadai Z, Pi HJ, Chevy Q, Ócsai K, Albeanu DF, Chiovini B, Szalay G, Katona G, Kepecs A, and Rózsa B (2022). Cortex-wide response mode of VIP-expressing inhibitory neurons by reward and punishment. Elife 11, e78815. 10.7554/eLife.78815. [PubMed: 36416886]
14. Batista-Brito R, Vinck M, Ferguson KA, Chang JT, Laubender D, Lur G, Mossner JM, Hernandez VG, Ramakrishnan C, Deisseroth K, et al. (2017). Developmental Dysfunction of VIP Interneurons Impairs Cortical Circuits. Neuron 95, 884–895.e9. 10.1016/j.neuron.2017.07.034. [PubMed: 28817803]
15. Karnani MM, Agetsuma M, and Yuste R (2014). A blanket of inhibition: functional inferences from dense inhibitory connectivity. Curr. Opin. Neurobiol 26, 96–102. 10.1016/j.conb.2013.12.015. [PubMed: 24440415]
16. Karnani MM, Jackson J, Ayzenshtat I, Tucciarone J, Manoocheri K, Snider WG, and Yuste R (2016). Cooperative Subnetworks of Molecularly Similar Interneurons in Mouse Neocortex. Neuron 90, 86–100. 10.1016/j.neuron.2016.02.037. [PubMed: 27021171]
17. Heintz TG, Hinojosa AJ, Dominiak SE, and Lagnado L (2022). Opposite forms of adaptation in mouse visual cortex are controlled by distinct inhibitory microcircuits. Nat. Commun 13, 1031. 10.1038/s41467-022-28635-8. [PubMed: 35210417]

18. Jackson J, Ayzenshtat I, Karnani MM, and Yuste R (2016). VIP+ interneurons control neocortical activity across brain states. J. Neurophysiol 115, 3008–3017. 10.1152/jn.01124.2015. [PubMed: 26961109]
19. Lee S, Kruglikov I, Huang ZJ, Fishell G, and Rudy B (2013). A disinhibitory circuit mediates motor integration in the somatosensory cortex. Nat. Neurosci 16, 1662–1670. 10.1038/nn.3544. [PubMed: 24097044]
20. Karnani MM, Jackson J, Ayzenshtat I, Hamzehei Sichani A, Manoocheri K, Kim S, and Yuste R (2016). Opening Holes in the Blanket of Inhibition: Localized Lateral Disinhibition by VIP Interneurons. J. Neurosci 36, 3471–3480. 10.1523/JNEUROSCI.3646-15.2016. [PubMed: 27013676]
21. Kuchibhotla KV, Gill JV, Lindsay GW, Papadoyannis ES, Field RE, Sten TAH, Miller KD, and Froemke RC (2017). Parallel processing by cortical inhibition enables context-dependent behavior. Nat. Neurosci 20, 62–71. 10.1038/nn.4436. [PubMed: 27798631]
22. Zhang S, Xu M, Kamigaki T, Hoang Do JP, Chang WC, Jenvay S, Miyamichi K, Luo L, and Dan Y (2014). Selective attention. Long-range and local circuits for top-down modulation of visual cortex processing. Science 345, 660–665. 10.1126/science.1254126. [PubMed: 25104383]
23. Jiang X, Shen S, Cadwell CR, Berens P, Sinz F, Ecker AS, Patel S, and Tolias AS (2015). Principles of connectivity among morphologically defined cell types in adult neocortex. Science 350, aac9462. 10.1126/science.aac9462. [PubMed: 26612957]
24. Hioki H, Okamoto S, Konno M, Kameda H, Sohn J, Kuramoto E, Fujiyama F, and Kaneko T (2013). Cell type-specific inhibitory inputs to dendritic and somatic compartments of parvalbumin-expressing neocortical interneuron. J. Neurosci 33, 544–555. 10.1523/JNEUROSCI.2255-12.2013. [PubMed: 23303934]
25. Walker F, Möck M, Feyerabend M, Guy J, Wagener RJ, Schubert D, Staiger JF, and Witte M (2016). Parvalbumin- and vasoactive intestinal polypeptide-expressing neocortical interneurons impose differential inhibition on Martinotti cells. Nat. Commun 7, 13664. 10.1038/ncomms13664. [PubMed: 27897179]
26. Chiu CQ, Martenson JS, Yamazaki M, Natsume R, Sakimura K, Tomita S, Tavalin SJ, and Higley MJ (2018). Input-Specific NMDAR-Dependent Potentiation of Dendritic GABAergic Inhibition. Neuron 97, 368–377.e3. 10.1016/j.neuron.2017.12.032. [PubMed: 29346754]
27. Garcia-Junco-Clemente P, Ikrar T, Tring E, Xu X, Ringach DL, and Trachtenberg JT (2017). An inhibitory pull-push circuit in frontal cortex. Nat. Neurosci 20, 389–392. 10.1038/nn.4483. [PubMed: 28114295]
28. Tyan L, Chamberland S, Magnin E, Camiré O, Francavilla R, David LS, Deisseroth K, and Topolnik L (2014). Dendritic inhibition provided by interneuron-specific cells controls the firing rate and timing of the hippocampal feedback inhibitory circuitry. J. Neurosci 34, 4534–4547. 10.1523/JNEUROSCI.3813-13.2014. [PubMed: 24671999]
29. Acsády L, Görcs TJ, and Freund TF (1996). Different populations of vasoactive intestinal polypeptide-immunoreactive interneurons are specialized to control pyramidal cells or interneurons in the hippocampus. Neuroscience 73, 317–334. 10.1016/0306-4522(95)00609-5. [PubMed: 8783252]
30. Acsády L, Arabadzisz D, and Freund TF (1996). Correlated morphological and neurochemical features identify different subsets of vasoactive intestinal polypeptide-immunoreactive interneurons in rat hippocampus. Neuroscience 73, 299–315. 10.1016/0306-4522(95)00610-9. [PubMed: 8783251]
31. Sadeh S, and Clopath C (2021). Inhibitory stabilization and cortical computation. Nat. Rev. Neurosci 22, 21–37. 10.1038/s41583-020-00390-z. [PubMed: 33177630]
32. Millman DJ, Ocker GK, Caldejon S, Kato I, Larkin JD, Lee EK, Luviano J, Nayan C, Nguyen TV, North K, et al. (2020). VIP interneurons in mouse primary visual cortex selectively enhance responses to weak but specific stimuli. Elife 9, e55130. 10.7554/eLife.55130. [PubMed: 33108272]
33. Litwin-Kumar A, Rosenbaum R, and Doiron B (2016). Inhibitory stabilization and visual coding in cortical circuits with multiple interneuron subtypes. J. Neurophysiol 115, 1399–1409. 10.1152/jn.00732.2015. [PubMed: 26740531]

34. Litwin-Kumar A, Oswald AMM, Urban NN, and Doiron B (2011). Balanced synaptic input shapes the correlation between neural spike trains. PLoS Comput. Biol 7, e1002305. 10.1371/journal.pcbi.1002305. [PubMed: 22215995]

35. Tsodyks MV, Skaggs WE, Sejnowski TJ, and McNaughton BL (1997). Paradoxical effects of external modulation of inhibitory interneurons. J. Neurosci 17, 4382–4388. 10.1523/JNEUROSCI.17-11-04382.1997. [PubMed: 9151754]

36. Ozeki H, Finn IM, Schaffer ES, Miller KD, and Ferster D (2009). Inhibitory stabilization of the cortical network underlies visual surround suppression. Neuron 62, 578–592. 10.1016/j.neuron.2009.03.028. [PubMed: 19477158]

37. Muñoz W, Tremblay R, Levenstein D, and Rudy B (2017). Layer-specific modulation of neocortical dendritic inhibition during active wakefulness. Science 355, 954–959. 10.1126/science.aag2599. [PubMed: 28254942]

38. Mesik L, Ma WP, Li LY, Ibrahim LA, Huang ZJ, Zhang LI, and Tao HW (2015). Functional response properties of VIP-expressing inhibitory neurons in mouse visual and auditory cortex. Front. Neural Circ 9, 22. 10.3389/fncir.2015.00022.

39. de Vries SEJ, Lecoq JA, Buice MA, Groblewski PA, Ocker GK, Oliver M, Feng D, Cain N, Ledochowitsch P, Millman D, et al. (2020). A large-scale standardized physiological survey reveals functional organization of the mouse visual cortex. Nat. Neurosci 23, 138–151. 10.1038/s41593-019-0550-9. [PubMed: 31844315]

40. Keller AJ, Dipoppa M, Roth MM, Caudill MS, Ingrosso A, Miller KD, and Scanziani M (2020). A Disinhibitory Circuit for Contextual Modulation in Primary Visual Cortex. Neuron 108, 1181–1193.e8. 10.1016/j.neuron.2020.11.013. [PubMed: 33301712]

41. Ayzenshtat I, Karnani MM, Jackson J, and Yuste R (2016). Cortical Control of Spatial Resolution by VIP+ Interneurons. J. Neurosci 36, 11498–11509. 10.1523/JNEUROSCI.1920-16.2016. [PubMed: 27911754]

42. Neske GT, and Connors BW (2016). Distinct Roles of SOM and VIP Interneurons during Cortical Up States. Front. Neural Circ 10, 52. 10.3389/fncir.2016.00052.

43. Kapfer C, Glickfeld LL, Atallah BV, and Scanziani M (2007). Supralinear increase of recurrent inhibition during sparse activity in the somatosensory cortex. Nat. Neurosci 10, 743–753. 10.1038/nn1909. [PubMed: 17515899]

44. Ma WP, Liu BH, Li YT, Huang ZJ, Zhang LI, and Tao HW (2010). Visual representations by cortical somatostatin inhibitory neurons–selective but with weak and delayed responses. J. Neurosci 30, 14371–14379. 10.1523/JNEUROSCI.3248-10.2010. [PubMed: 20980594]

45. Silberberg G, and Markram H (2007). Disynaptic inhibition between neocortical pyramidal cells mediated by Martinotti cells. Neuron 53, 735–746. 10.1016/j.neuron.2007.02.012. [PubMed: 17329212]

46. Yang CF, Chiang MC, Gray DC, Prabhakaran M, Alvarado M, Juntti SA, Unger EK, Wells JA, and Shah NM (2013). Sexually dimorphic neurons in the ventromedial hypothalamus govern mating in both sexes and aggression in males. Cell 153, 896–909. 10.1016/j.cell.2013.04.017. [PubMed: 23663785]

47. Vinck M, Batista-Brito R, Knoblich U, and Cardin JA (2015). Arousal and locomotion make distinct contributions to cortical activity patterns and visual encoding. Neuron 86, 740–754. 10.1016/j.neuron.2015.03.028. [PubMed: 25892300]

48. Niell CM, and Stryker MP (2010). Modulation of visual responses by behavioral state in mouse visual cortex. Neuron 65, 472–479. 10.1016/j.neuron.2010.01.033. [PubMed: 20188652]

49. Cardin JA, Carlén M, Meletis K, Knoblich U, Zhang F, Deisseroth K, Tsai LH, and Moore CI (2009). Driving fast-spiking cells induces gamma rhythm and controls sensory responses. Nature 459, 663–667. 10.1038/nature08002. [PubMed: 19396156]

50. Cardin JA (2018). Inhibitory Interneurons Regulate Temporal Precision and Correlations in Cortical Circuits. Trends Neurosci 41, 689–700. 10.1016/j.tins.2018.07.015. [PubMed: 30274604]

51. Veit J, Handy G, Mossing DP, Doiron B, and Adesnik H (2023). Cortical VIP neurons locally control the gain but globally control the coherence of gamma band rhythms. Neuron 111, 405–417.e5. 10.1016/j.neuron.2022.10.036. [PubMed: 36384143]

52. Cohen MR, and Kohn A (2011). Measuring and interpreting neuronal correlations. Nat. Neurosci 14, 811–819. 10.1038/nn.2842. [PubMed: 21709677]

53. Adesnik H, Bruns W, Taniguchi H, Huang ZJ, and Scanziani M (2012). A neural circuit for spatial summation in visual cortex. Nature 490, 226–231. 10.1038/nature11526. [PubMed: 23060193]

54. Mahn M, Gibor L, Patil P, Cohen-Kashi Malina K, Oring S, Printz Y, Levy R, Lampl I, and Yizhar O (2018). High-efficiency optogenetic silencing with soma-targeted anion-conducting channelrhodopsins. Nat. Commun 9, 4125. 10.1038/s41467-018-06511-8. [PubMed: 30297821]

55. Mossner JM, Batista-Brito R, Pant R, and Cardin JA (2020). Developmental loss of MeCP2 from VIP interneurons impairs cortical function and behavior. Elife 9, e55639. 10.7554/eLife.55639. [PubMed: 32343226]

56. Lur G, Vinck MA, Tang L, Cardin JA, and Higley MJ (2016). Projection-Specific Visual Feature Encoding by Layer 5 Cortical Subnetworks. Cell Rep 14, 2538–2545. 10.1016/j.celrep.2016.02.050. [PubMed: 26972011]

57. Doiron B, Litwin-Kumar A, Rosenbaum R, Ocker GK, and Josić K (2016). The mechanics of state-dependent neural correlations. Nat. Neurosci 19, 383–393. 10.1038/nn.4242. [PubMed: 26906505]

58. Stringer C, Pachitariu M, Steinmetz NA, Okun M, Bartho P, Harris KD, Sahani M, and Lesica NA (2016). Inhibitory control of correlated intrinsic variability in cortical networks. Elife 5, e19695. 10.7554/eLife.19695. [PubMed: 27926356]

59. Sabatini BL (2019). The impact of reporter kinetics on the interpretation of data gathered with fluorescent reporters. Preprint at bioRxiv 10.1101/834895.

60. Pachitariu M, Stringer C, and Harris KD (2018). Robustness of Spike Deconvolution for Neuronal Calcium Imaging. J. Neurosci 38, 7976–7985. 10.1523/JNEUROSCI.3339-17.2018. [PubMed: 30082416]

61. Huang L, Ledochowitsch P, Knoblich U, Lecoq J, Murphy GJ, Reid RC, de Vries SE, Koch C, Zeng H, Buice MA, et al. (2021). Relationship between simultaneously recorded spiking activity and fluorescence signal in GCaMP6 transgenic mice. Elife 10, e51675. 10.7554/eLife.51675. [PubMed: 33683198]

62. Wei Z, Lin BJ, Chen TW, Daie K, Svoboda K, and Druckmann S (2020). A comparison of neuronal population dynamics measured with calcium imaging and electrophysiology. PLoS Comput. Biol 16, e1008198. 10.1371/journal.pcbi.1008198. [PubMed: 32931495]

63. Cone JJ, Scantlen MD, Histed MH, and Maunsell JHR (2019). Different Inhibitory Interneuron Cell Classes Make Distinct Contributions to Visual Contrast Perception. eNeuro 6, 18.2019, ENEURO.0337. 10.1523/ENEURO.0337-18.2019.

64. Chen TW, Wardill TJ, Sun Y, Pulver SR, Renninger SL, Baohan A , Schreiter ER, Kerr RA, Orger MB, Jayaraman V, et al. (2013). Ultrasensitive fluorescent proteins for imaging neuronal activity. Nature 499, 295–300. 10.1038/nature12354. [PubMed: 23868258]

65. Dubbs A, Guevara J, and Yuste R (2016). moco: Fast Motion Correction for Calcium Imaging. Front Neuroinform 10, 6. 10.3389/fninf.2016.00006. [PubMed: 26909035]

66. Fründ I, Haenel NV, and Wichmann FA (2011). Inference for psychometric functions in the presence of nonstationary behavior. J. Vis 11, 16. 10.1167/11.6.16.

67. Rigby RA, and Stasinopoulos DM (2005). Generalized additive models for location, scale and shape,(with discussion). Applied Statistics 54, 507–554.

68. Tang L, and Higley MJ (2020). Layer 5 Circuits in V1 Differentially Control Visuomotor Behavior. Neuron 105, 346–354.e5. 10.1016/j.neuron.2019.10.014. [PubMed: 31757603]

69. Friedrich J, Zhou P, and Paninski L (2017). Fast online deconvolution of calcium imaging data. PLoS Comput. Biol 13, e1005423. 10.1371/journal.pcbi.1005423. [PubMed: 28291787]

Highlights

- VIP interneurons regulate the state-dependent modulation of SST interneurons
- VIP interneurons control visual feature selectivity in SST interneurons and excitatory neurons
- The impact of VIP interneuron activity on visual perceptual performance varies with context

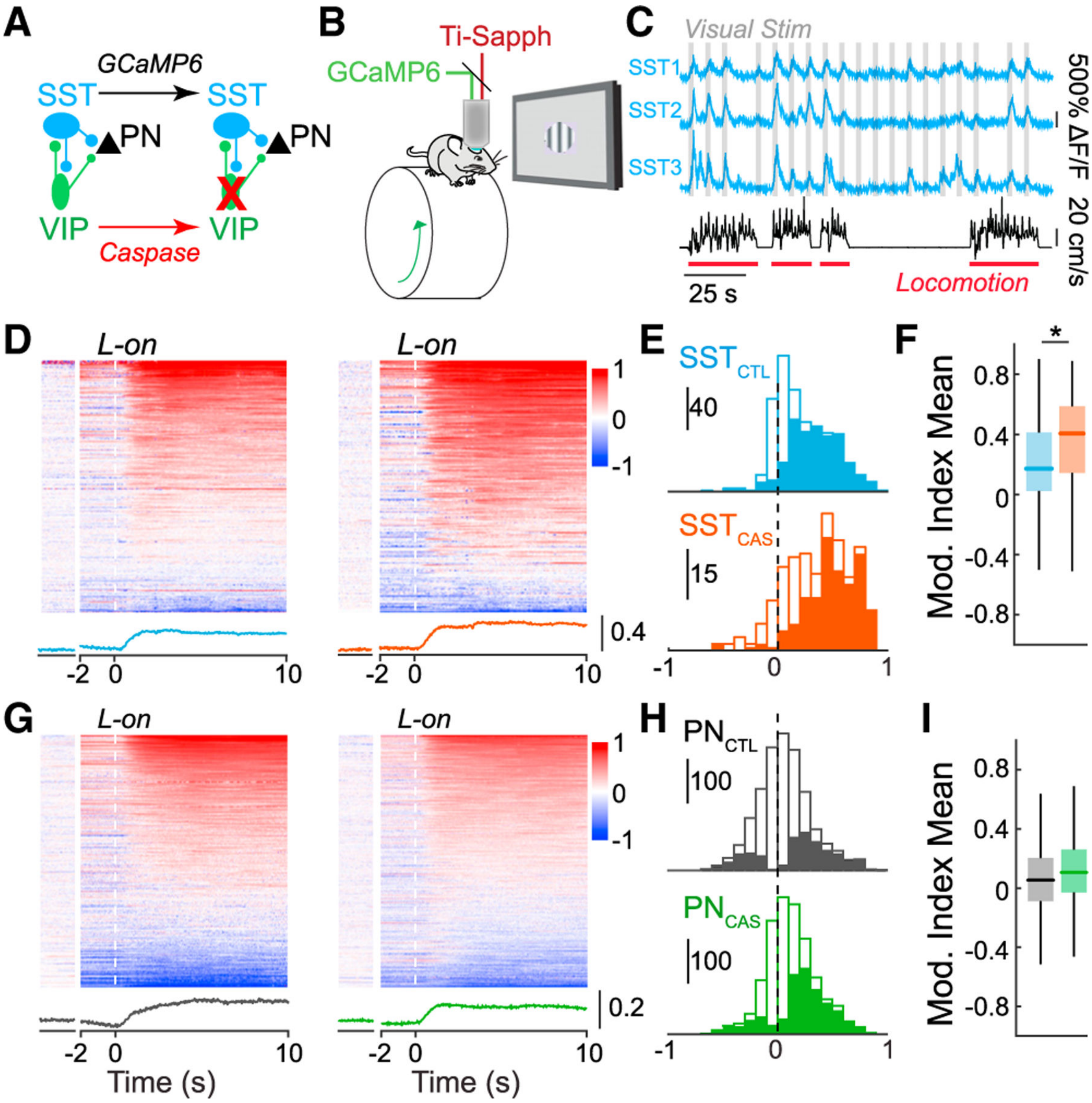

Figure 1. VIP interneuron ablation selectively disrupts state-dependent activity of SST interneurons

(A) Cre-dependent expression of caspase-3 causes cell death in VIP-INs. GCaMP6 is expressed in SST-INs or PNs in each experiment.

(B) Schematic of the *in vivo* 2-photon imaging configuration.

(C) Ca2+ traces of three example SST-INs (blue) recorded during the presentation of visual stimuli (gray) and wheel speed tracking (black) to identify locomotion bouts (red).

(D) Modulation of activity around locomotion onset (L-on), calculated as an index value, of SST-INs in control animals (left) and VIP-ablation animals (right). Modulation during periods of sustained quiescence (Q) (see STAR Methods) is shown to the left for comparison. Average modulation trace shown below heatmaps for controls (blue) and VIP-ablation animals (orange).

(E) Histogram of modulation indices of all SST-INs in control (SST_{CTL}, blue; n = 600 cells in 7 mice) and VIP-ablation animals (SST_{CAS}, orange; n = 277 cells in 5 mice). Solid bars indicate cells showing significant modulation at $p < 0.05$ (shuffle test).

(F) Boxplot of L modulation indices in (E). Central mark indicates the median, and whiskers indicate 25th and 75th percentiles.

(G–I) Same analysis as in (D)–(F) but for PNs in control (PN_{CTL}, black; n = 1679 cells in 6 mice) and VIP-IN ablation animals (PN_{CAS}, green; n = 1585 cells in 6 mice). $^{*}p < 0.05$, linear mixed-effects model.

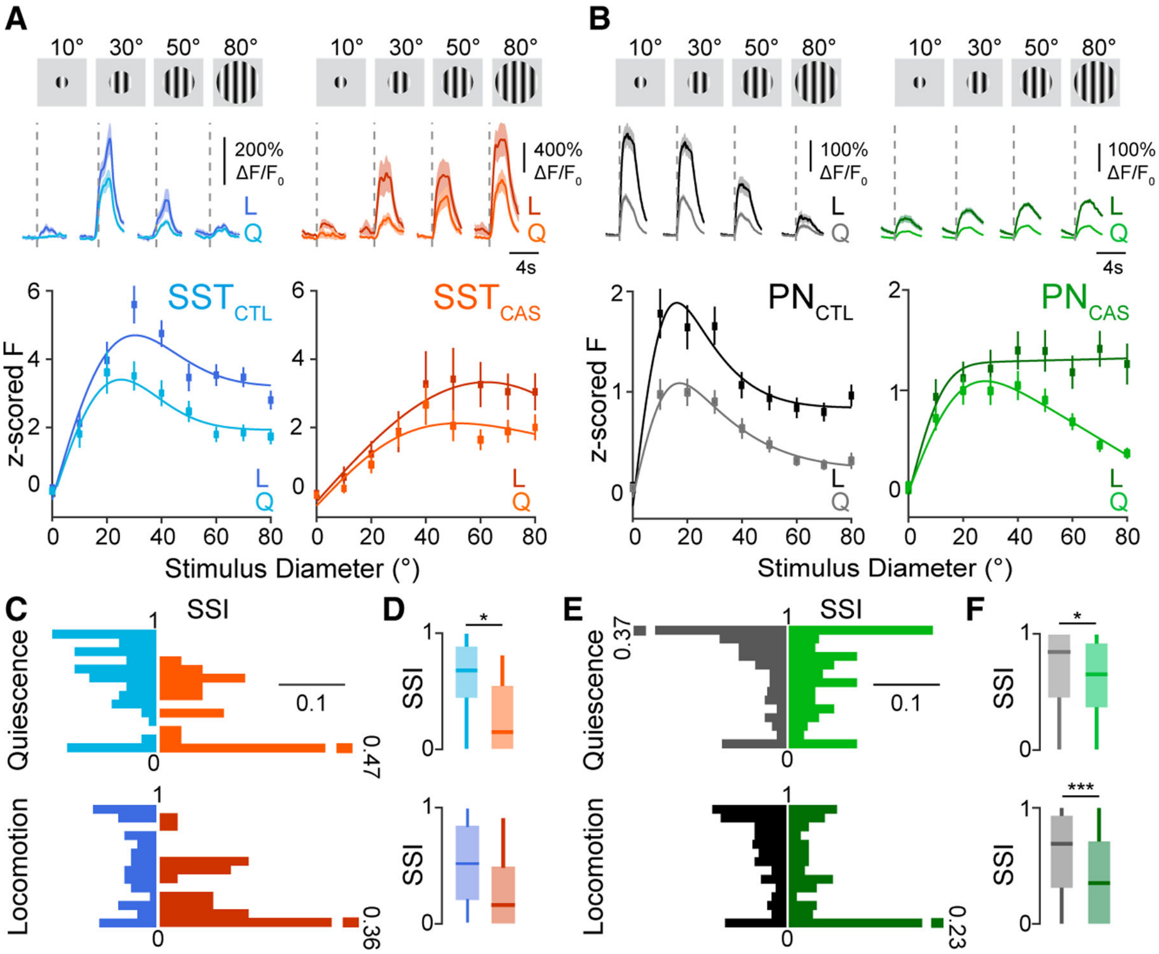

Figure 2. VIP interneuron ablation alters the size-tuning properties of SST-INs and PNs

(A) Top: responses of example SST-INs to drifting grating stimuli of varying sizes in a control (left, blue; SST$_{CTL}$) and a VIP-ablation animal (right, orange; SST$_{CAS}$). Vertical dashed lines indicate visual stimulus onset. Responses during quiescence (Q,light traces) are shown separately from those during locomotion (L,dark traces). Shaded areas indicate mean ± SEM. Bottom: visual responses of SST cells Z scored to the 1 s baseline period before the stimulus onset for periods of Q (light lines) and L (dark lines) for control (blue) and VIP-ablation animals (orange).

(B) Same as in (A) but for PNs in control (gray; PN$_{CTL}$) and VIP-ablation (green; PN$_{CAS}$) animals.

(C) Probability distribution of the surround suppression index (SSI), separated by L state, for SST-INs in control (blue; Q [top]: n = 86 cells, 6 mice; L [bottom]: n = 101 cells, 6 mice) and VIP-ablation animals (orange; Q [top]: n = 36 cells, 4 mice; L [bottom]: n = 30 cells, 4 mice).

(D) Boxplot of the SSI during Q (top) and L (bottom).

(E and F) Same as in (C) and (D) but for PNs in control (gray; Q [top]: n = 279 cells, 6 mice; L [bottom]: n = 314 cells, 6 mice) and VIP-ablation (green; Q [top]: n = 175 cells, 5 mice; L [bottom]: n = 165 cells, 5 mice) animals. *$p < 0.05$, ***$p < 0.001$, 0/1 inflated beta mixed-effects regression model, with experiment type (control or VIP ablation) as fixed effect and mouse with nested imaging field of view as random effect.

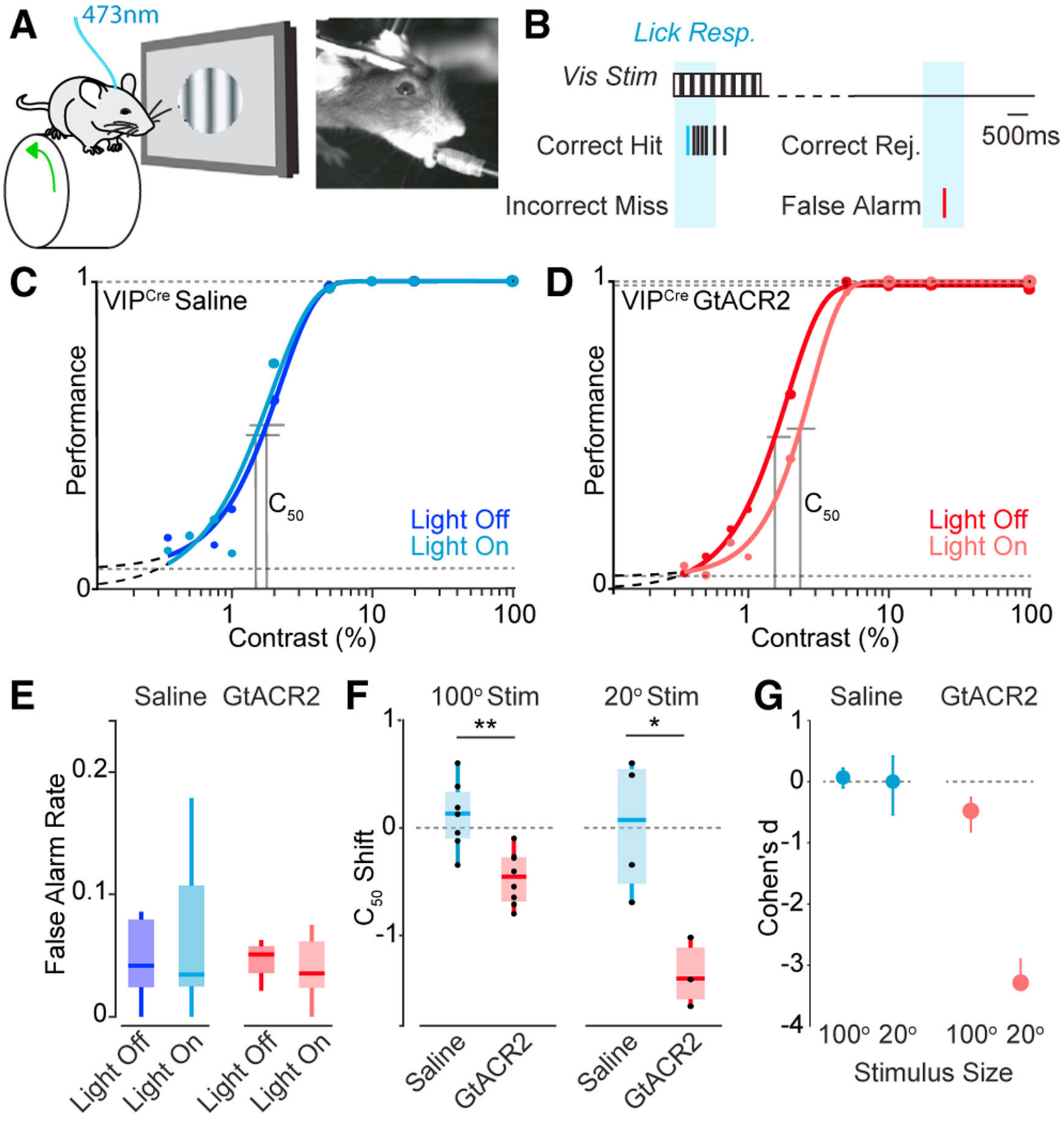

Figure 3. VIP-INs regulate visual perception in a size-dependent manner

(A) Schematic of experimental paradigm with a freely running head-fixed mouse, lick spout, visual stimulation, and 473 nm optogenetic stimulation.

(B) Schematic of visual detection task.

(C) Psychometric responses for a representative mouse injected with saline. Darker shade indicates control trials, and lighter shade indicates trials with light pulse. The C_{50} is represented by vertical lines.

(D) Psychometric responses for a representative mouse injected with the GtACR2 opsin for VIP inhibition upon light stimulation.

(E) False alarm rates for control (saline) and GtACR2 mice.

(F) C_{50} shift (light off C_{50} – light on C_{50}) for control and GtACR2 animals for small- (20°) and large-diameter (100°) stimuli.

(G) Cohen’s d effect size for small (20°) and large (100°) stimuli. 100° stimulus experiments: n = 7 control, 8 GtACR2 mice. 20° stimulus experiments: n = 4 control, 3 GtACR2 mice. $*p < 0.05$, $**p < 0.01$, Student’s t test.

Summary of all statistical tests

Figure	Comparison	N	Test	Estimate	t stat	CI	p value
1F	comparison of locomotion modulation indices for SST control and SST with VIP ablated	Ctrl: 7 mice, 600 cells w/out VIP: 5 mice, 277 cells	linear mixed-effects model $y \sim \text{experiment type} + (1 \mid \text{mouse:FoV})$	0.140	2.566	[0.033, 0.247]	0.010[a]
1I	comparison of locomotion modulation indices for PN control and PN with VIP ablated	Ctrl: 6 mice, 1,679 cells w/out VIP: 6 mice, 1,585 cells	linear mixed-effects model $y \sim \text{experiment type} + (1 \mid \text{mouse:FoV})$	0.048	1.726	[−0.007, 0.104]	0.084
2D, top	comparison of surround suppression indices during quiescence (Q) for SST control and SST with VIP ablated	Ctrl: 6 mice, 86 cells w/out VIP: 4 mice, 30 cells	zero/one inflated beta mixed-effects regression model (experiment type as fixed effect; mouse with nested FoV as random effects)	−0.930	−3.620	[−1.439, −0.422]	<0.001[a]
2D, bottom	comparison of surround suppression indices during locomotion (L) for SST control and SST with VIP ablated	Ctrl: 6 mice, 101 cells w/out VIP: 4 mice, 36 cells	zero/one inflated beta mixed-effects regression model (experiment type as fixed effect; mouse with nested FoV as random effects)	−0.217	−0.909	[−0.684, 0.250]	0.366
2F, top	comparison of surround suppression indices during Q for PN control and PN with VIP ablated	Ctrl: 6 mice, 279 cells w/out VIP: 5 mice, 175 cells	zero/one inflated beta mixed-effects regression model (experiment type as fixed effect; mouse with nested FoV as random effects)	−0.545	−4.288	[−0.795, −0.295]	<0.001[a]
2F, bottom	comparison of surround suppression indices during L for PN control and PN with VIP ablated	Ctrl: 6 mice, 314 cells w/out VIP: 5 mice, 165 cells	zero/one inflated beta mixed-effects regression model (experiment type as fixed effect; mouse with nested FoV as random effects)	−0.423	−2.775	[−0.724, −0.123]	0.006[a]
3E, left	comparison of false alarm rates for saline-injected mice during light-stimulation-on trials and light-off trials	7 mice	paired t test	N/A	N/A	[−0.063, 0.052]	0.812
3E, right	comparison of false alarm rates for GtACR2-injected mice during light-stimulation-on trials and light-off trials	8 mice	paired t test	N/A	N/A	[−0.019, 0.040]	0.444

Figure	Comparison	N	Test	Estimate	t stat	CI	p value
3F, left	comparison of C_{50} shift for saline-injected and GtACR2-injected (opto) mice for 100° stimuli	saline: 7 mice; GtACR2: 8 mice	unpaired t test	N/A	N/A	[0.268, 0.897]	0.002^{a}
3F, right	comparison of C_{50} shift for saline-injected and GtACR2-injected (opto) mice for 20° stimuli	saline: 4 mice; GtACR2: 3 mice	unpaired t test	N/A	N/A	[0.338, 2.459]	0.019
S1C, left	comparison of VIP cell density in control and VIP-ablated mice 10 days post-injection	saline: 3 mice; caspase: 3 mice	unpaired t test	N/A	N/A	[−51.53, 175.52]	0.204
S1C, middle	comparison of VIP cell density in control and VIP-ablated mice 14 days post-injection	saline: 3 mice; caspase: 3 mice	unpaired t test	N/A	N/A	[76.07, 283.96]	0.009^{a}
S1C, right	comparison of VIP cell density in control and VIP-ablated mice 21 days post-injection	saline: 3 mice; caspase: 3 mice	unpaired t test	N/A	N/A	[148.66, 275.64]	$<0.001^{a}$
S1D	comparison of VIP cell density in behavioral control mice and behavioral VIP-ablated mice	saline: 4 mice; caspase: 4 mice	unpaired t test	N/A	N/A	[151.21, 309.09]	$<0.001^{a}$
S1E, left	noise correlations of SST $\Delta F/F_0$	Ctrl: 6 mice, 2,180 cell pairs w/out VIP: 4 mice, 447 cell pairs	linear mixed-effects model y ~ 1 + state*experiment type + (1 | mouse:FoV)	$\beta state = 0.045$ $\beta exp = -0.031$ $\beta state*exp = 0.071$	4.282 −0.580 2.812	[0.024, 0.065] [−0.135, 0.073] [0.022, 0.121]	$<0.001^{a}$ 0.562 0.005^{a}
S1E, right	noise correlations of PN $\Delta F/F_0$	Ctrl: 5 mice, 1,077 cell pairs w/out VIP: 6 mice, 2,481 cell pairs	linear mixed-effects model y ~ 1 + state*experiment type + (1 | mouse:FoV)	$\beta state = 0.007$ $\beta exp = 0.023$ $\beta state*exp = 0.024$	0.569 1.130 1.763	[−0.016, 0.029] [−0.017, 0.064] [−0.003, 0.051]	0.569 0.259 0.078
S1F, left	noise correlations of SST deconvolved $\Delta F/F_0$	Ctrl: 6 mice, 2,180 pairs w/out VIP: 4 mice, 447 pairs	linear mixed-effects model y ~ 1 + state*experiment type + (1 | mouse:FoV)	$\beta state = -0.011$ $\beta exp = -0.027$ $\beta state*exp = 0.099$	−1.424 −0.640 5.322	[−0.026, 0.004] [−0.112, 0.057] [0.062, 0.135]	0.155 0.522 $<0.001^{a}$

Figure	Comparison	N	Test	Estimate	t stat	CI	p value
S1F, right	noise correlations of PN deconvolved $\Delta F/F_0$	Ctrl: 5 mice, 1,077 pairs w/out VIP: 6 mice, 2,481 pairs	linear mixed-effects model y ~ 1 + state*experiment type + (1 | mouse:FoV)	*βstate* = −0.016 *βexp* = −0.019 *βstate*exp* = 0.015	−1.671 −2.337 1.336	[−0.035, 0.003] [−0.035, −0.003] [−0.007, 0.038]	0.095 0.020 0.181
S1G and S1H, left	noise correlations of SST mean-matched deconvolved $\Delta F/F_0$	Ctrl: 6 mice, (1,293, 975) (Q, L) pairs w/out VIP: 4 mice, (261, 202) (Q, L) pairs	linear mixed-effects model y ~ 1 + state*experiment type + (1 | mouse:FoV)	*βstate* = −0.024 *βexp* = −0.014 *βstate*exp* = 0.098	−1.476 −0.262 3.176	[−0.056, 0.008] [−0.120, 0.092] [0.037, 0.158]	0.140 0.793 0.0015[a]
S1G and S1H, right	noise correlations of PN mean-matched deconvolved $\Delta F/F_0$	Ctrl: 6 mice, (748, 748) (Q, L) pairs w/out VIP: 6 mice, (1,658, 1786) (Q, L) pairs	linear mixed-effects model y ~ 1 + state*experiment type + (1 | mouse:FoV)	*βstate* = −0.017 *βexp* = −0.015 *βstate*exp* = 0.011	−1.523 −1.508 0.846	[−0.039, 0.005] [−0.033, 0.004] [−0.015, 0.038]	0.128 0.132 0.398
S2B	comparison of percentage of visually tuned cells of all visually responsive cells in SST controls and SST with VIP ablated	Ctrl: 6 mice w/out VIP: 4 mice	unpaired t test	N/A	2.844	[0.060, 0.577]	0.022[a]
S2D	comparison of percentage of visually tuned cells of all visually responsive cells in PN controls and PN with VIP ablated	Ctrl: 6 mice w/out VIP: 5 mice	unpaired t test	N/A	1.582	[−0.052, 0.296]	0.148
S2F, top	comparison of preferred size of visual responses during Q in SST controls and SST with VIP ablated	Ctrl: 6 mice, 86 cells w/out VIP: 4 mice, 30 cells	zero/one inflated beta mixed-effects regression model (experiment type as fixed effect; mouse with nested FoV as random effects)	43.12	2.971	[14.67, 71.57]	0.004[a]
S2F, bottom	comparison of preferred size of visual responses during L in SST controls and SST with VIP ablated	Ctrl: 4 mice, 66 cells w/out VIP: 4 mice, 21 cells	zero/one inflated beta mixed-effects regression model (experiment type as fixed effect; mouse with nested FoV as random effects)	10.74	0.605	[−24.06, 45.54]	0.547
S2H, top	comparison of preferred size of visual responses during Q in PN	Ctrl: 6 mice, 254 cells, w/out VIP: 5 mice, 175 cells	zero/one inflated beta mixed-effects regression model (experiment type as fixed effect; mouse with nested FoV as random effects)	22.70	3.040	[8.07, 38.33]	0.003[a]

Figure	Comparison	N	Test	Estimate	t stat	CI	p value
	controls and PN with VIP ablated						
S2H, bottom	comparison of preferred size of visual responses during L in PN controls and PN with VIP ablated	Ctrl: 3 mice, 202 cells w/out VIP: 3 mice, 122 cells	zero/one inflated beta mixed-effects regression model (experiment type as fixed effect; mouse with nested FoV as random effects)	1.89	0.201	[−16.49, 20.27]	0.841
S2J, top	comparison of surround suppression indices during Q for all visually responsive (tuned and untuned) SST control and SST with VIP ablated	Ctrl: 6 mice, 134 cells w/out VIP: 4 mice, 69 cells	zero/one inflated beta mixed-effects regression model (experiment type as fixed effect; mouse with nested FoV as random effects)	−1.305	−6.101	[−1.724, −0.885]	<0.001[a]
S2J, bottom	comparison of surround suppression indices during L for all visually responsive (tuned and untuned) SST control and SST with VIP ablated	Ctrl: 6 mice, 121 cells w/out VIP: 4 mice, 53 cells	zero/one inflated beta mixed-effects regression model (experiment type as fixed effect; mouse with nested FoV as random effects)	−0.651	−2.752	[−1.115, −0.187]	0.007[a]
S2L, top	comparison of surround suppression indices during Q for all visually responsive (tuned and untuned) PN control and PN with VIP ablated	Ctrl: 6 mice, 379 cells w/out VIP: 5 mice, 243 cells	zero/one inflated beta mixed-effects regression model (experiment type as fixed effect; mouse with nested FoV as random effects)	−0.671	−6.384	[−0.877, −0.465]	<0.001[a]
S2L, bottom	comparison of surround suppression indices during L for all visually responsive (tuned and untuned) PN control and PN with VIP ablated	Ctrl: 6 mice, 479 cells w/out VIP: 5 mice, 234 cells	zero/one inflated beta mixed-effects regression model (experiment type as fixed effect; mouse with nested FoV as random effects)	−0.459	−4.229	[−0.672, −0.247]	<0.001[a]
S3F	comparison of modulation indices in response to various light intensities	1 mouse, 84 units	Friedman's ANOVA and post-hoc Wilcoxon signed rank test	N/A	N/A	N/A	$p_{LOW\text{-}MED}$ < 0.001[a] $p_{MED\text{-}HIGH}$ < 0.001[a] $p_{LOW\text{-}HIGH}$ < 0.001[a]
S3H		comparison of run probability in saline-injected and GtACR2-injected mice	saline: 7 mice GtACR2: 8 mice	linear mixed-effects model $y \sim \text{experiment type} + (1 \mid \text{mouse:FoV})$	0.068	0.742	[−0.114, 0.250] 0.460

Figure	Comparison	N	Test	Estimate	t stat	CI	p value
S3I, left	comparison of C_{50} shift for saline-injected and GtACR2-injected (opto) mice during Q	saline: 7 mice GtACR2: 8 mice	unpaired t test	N/A	3.615	[0.276, 1.094]	0.003[a]
S3I, right	comparison of C_{50} shift for saline-injected and GtACR2-injected (opto) mice during L	saline: 7 mice GtACR2: 8 mice	unpaired t test	N/A	1.263	[−0.239, 0.913]	0.229
S3J, left	comparison of C_{50} for light-stimulation-on trials and light-off trials in GtACR2 mice for 100° stimuli	GtACR2: 8 mice	paired t test	N/A	−5.394	[−0.675, −0.263]	0.001[a]
S3J, right	comparison of C_{50} for light-stimulation-on trials and light-off trials in GtACR2 mice for 20° stimuli	GtACR2: 3 mice	paired t test	N/A	−7.273	[−2.189, −0.562]	0.018[a]
S3K, left	Comparison of C_{50} for light-stimulation-on trials and light-off trials in saline mice for 100° stimuli	saline: 7 mice	paired t test	N/A	0.944	[−0.181, 0.407]	0.382
S3K, right	comparison of C_{50} for light-stimulation-on trials and light-off trials in saline mice for 20° stimuli	saline: 4 mice	paired t test	N/A	0.072	[−1.001, 1.048]	0.947
S3N	comparison of run probability in saline-injected and VIP-ablated mice	Ctrl (saline): 14 mice w/out VIP: 8 mice	linear mixed-effects model $y \sim \text{experiment type} + (1 \mid \text{mouse:FoV})$	0.0319	0.729	[−0.054, 0.118]	0.467
S3O, left	comparison of C_{50} for saline-injected and VIP-ablated mice during Q	Ctrl (saline): 14 mice w/out VIP: 8 mice	unpaired t test	N/A	−2.231	[−1.655, −0.056]	0.037[a]
S3O, right	comparison of C_{50} for saline-injected and VIP-ablated mice during L	Ctrl (saline): 14 mice w/out VIP: 8 mice	unpaired t test	N/A	−1.403	[−2.054, 0.402]	0.176
S3P	comparison of lick probability for lowest contrast stimuli in	Ctrl (saline): 14 mice w/out VIP: 8 mice	unpaired t test	N/A	1.663	[−0.010, 0.095]	0.109

Figure	Comparison	N	Test	Estimate	t stat	CI	p value
	saline-injected and VIP-ablated mice						

Ctrl, control; w/out, without; FoV, field of vision.

[a] $p < 0.05$

KEY RESOURCES TABLE

REAGENT or RESOURCE	**SOURCE**	**IDENTIFIER**
Bacterial and virus strains		
AAVdj-ef1a-fDIO-GCaMP6m	plasmid gift of K. Deisseroth lab, Stanford	N/A
AAV5-Syn-GCaMP6s	Chen et al., 2013[64]	Addgene # 100843
AAV5-Syn-FLEX-GCaMP6s	Chen et al., 2013[64]	Addgene # 100845
AAV5 ef1a-Flex-taCasP3-TEVP	Yang et al., 2013[46]	UNC Vector Core
AAV1-hSyn1-SIO-stGtACR2-FusionRed	Mahn et al., 2018[54]	Addgene #105677
Experimental models: Organisms/strains		
Mouse VIP-IRES-Cre$^{+/0}$ (C57BL/6J)	Jackson Laboratory	JAX 031628
Mouse Emx1-IRES-Cre$^{+/0}$	Jackson Laboratory	JAX 005628
Mouse Sst-IRES-Flp$^{+/0}$	Jackson Laboratory	JAX 031629
Mouse Ai9	Jackson Laboratory	JAX 007909
Mouse Sst-IRES-Cre$^{+/0}$	Jackson Laboratory	JAX 018973
Mouse Ai148(TIT2L-GC6f-ICL-tTA2)-D	Jackson Laboratory	JAX 030328
Software and algorithms		
MATLAB R2022b (with curve fitting toolbox)	Mathworks	https://www.mathworks.com/
ImageJ Moco Algorithm	Dubbs et al., 2016[65]	https://github.com/NTCColumbia/moco
R (v. 2022.7.2.576)	R Core Team (2022)	https://www.R-project.org/
MATLAB psignifit toolbox	Frund et al., 2011[66]	https://github.com/wichmann-lab/psignifit
R GAMLSS package	Rigby and Stasinopoulos, 2005[67]	https://cran.r-project.org/web/packages/gamlss/index.html
Custom code	This paper	https://github.com/cardin-higley-lab/Ferguson_et_al_2023 https://doi.org/10.5281/zenodo.8205650